Standalone brushless motor module optimized for legged robots

Piotr WASILEWSKI[1] and Rafal GRADZKI [2*]

[1] Bialystok University of Technology, Faculty of Electrical Engineering, Wiejska 45D, 15-351 Bialystok, Poland
[2] Bialystok University of Technology, Faculty of Mechanical Engineering, Department of Robotics and Mechatronics,
Wiejska 45C, 15-351 Bialystok, Poland

Abstract. The main focus of the article is an advanced actuator, designed and optimized for small dynamic legged robots. The presented actuator prototype is unique, as the market lacks similar solutions when dimensions and weight of the module are considered. The actuator has a modular structure, which makes it easy to replace in case of malfunction and simplifies the overall structure of the robot. High torque bandwidth, achieved by the module, is crucial to agile locomotion, obstacle avoidance and push recovery of the quadrupedal robot. The Authors have conducted a solution review aimed at similar small-size modules. It was found that there are no advanced actuators suitable for sub 5 kg quadruped robots. The unique design presented in this paper is described in all three aspects: mechanical, electrical and software. The mechanical section depicts the solutions implemented in the module, especially the low gear ratio gearbox. The custom brushless motor driver is presented in the electrical section, together with detailed diagrams and hardware descriptions. The last section depicts solutions implemented in the software, the main motor control algorithm and auxiliary modules such as automatic motor parameter identification and encoder misalignment correction. Tests performed in the last part of this paper validated the design goals established for the actuator. The results confirmed the high torque capability and exhibited the motor saturation region. Continuous and peak torque were measured based on the thermal characteristics of the module. Moreover, the automatic motor parameter identification process carried out by the controller itself was validated by manual measurements.

Key words: brushless motor; quadruped robot; actuator module.

1. INTRODUCTION

Quadruped robots have many applications, especially in environments dangerous for people [1]. They were originally designed to carry heavy equipment for military purposes [2] in difficult terrain, unreachable by wheeled machines or flying robots. Recently, walking robots manufactured by Boston Dynamics [3] company were used for inspecting the SpaceX's Starship fuel tank while refueling with highly explosive liquid propellants [4], as it was too dangerous to be supervised by staff. At the same time, Boston Dynamic's quadrupedal robots patrolled Singapore city parks to watch if people obey the social distancing restrictions introduced due to the COVID-19 pandemic [5]. These examples show that there is a need for robust inspection machines able to locomote in diverse terrain. Legged robots are a great solution to this problem as they can perform monotonous tasks in demanding environments with great precision and repeatability.

To achieve high robustness and agility, walking robots have to be equipped with high-end actuators [6]. Desired features are: high torque, low inertia, low mass, and the ability to read the reaction torques [7]. Due to these requirements, special actuators are designed, most often based on brushless motors.

This choice is dictated by their high torque density and low overall mass in comparison to the power capability. Their durability is limited only by the bearings and possible winding overheat events. When combined with a low ratio, easily back drivable gearbox, it is possible to utilize torque measurements based solely on the motor phase current measurements [8].

The market of highly dynamic actuators for walking robots is still fairly new and constantly growing. However, it is possible to distinguish a few of the most advanced solutions used in quadrupedal robots these days, both professional and experimental.

Anybotic's ANYdrive motor [9] – the actuator is based on a brushless motor integrated with a backlash-free gearbox and a power electronic module to control the motor. High impact robustness and precision torque control are guaranteed thanks to a built-in spring in series with the actuator output. The deflection of the spring is converted to a torque measurement, while at the same time the actuator is protected against sudden impact. The drawback of this solution is that it influences the torque control bandwidth, reducing it significantly. Moreover, the torque sensing spring requires precision machining processes and trimming routines to maintain similar readings between different modules. The module weights around 900g and is able to achieve 40 Nm peak torque.

Unitree A1 actuator [10] – a high-performance brushless motor module with a build-in planetary reducer. Equipped with a 15-bit encoder ensures precision positioning. The output

Bull. Pol. Acad. Sci. Tech. Sci., vol. 70, no. 2, p. e141008, 2022

1

torque is calculated based on motor phase currents, thus there is no need for complex torque-sensing structures. The actuator is dust-proof and resistant to shocks. Moreover, the stator is able to dissipate heat through the motor casing, which is designed for the eventual external radiator mount. The 600 g module is able to generate up to 33.5Nm peak torque at 40 A. The A1 quadruped robot shows remarkable maneuvers on the video clips published by the company.

Minicheetach actuator – an optimized brushless actuator based on a large diameter quadrocopter brushless motor, and a planetary gearbox integrated into the stator [11]. This unusual placement of the gearbox results in the reduced height of the module making it a low profile disc. This way, it is convenient to integrate into a quadruped leg structure. It is capable of high bandwidth torque control thanks to a rigid structure with no additional series elastic elements [12]. It weighs around 480g and is capable of producing 17 Nm peak torque. Similar to the A1 actuator, it utilizes a motor phase currents sensing method for measuring the output torque. Thanks to the low overall cost, high performance, and relatively easy to manufacture aluminum parts, the actuator is widely copied by many third parties all over the world. The module was used in the Minicheetach quadruped robot which is the first robot in the world to perform a full 360° backflip.

Open Torque actuator – ultra-light design implementing brushless motors with 9:1 geared belt gearbox design [13]. The module is oblong and at the same time serves as part of the leg structure. Most of the parts are 3d printed for reducing the weight. The authors use external force sensors for detecting leg tip touchdowns as they claim the motor phase current-based detection is much slower.

Although the existence of a few walking robot actuators, there is still a demand for a smaller actuator, which could be used in low-cost small educational robots [14]. Actuators presented in the first section are rather large – more than 90 mm in diameter and more than 500 g in mass. Their big form factor makes them useful only in medium-size machines – of over 9 kg. They are capable of producing large torques, which can be dangerous in case of a fault and cause severe injuries. A lot of manufacturing cost is related to the usage of 5-axis milling machines due to complicated parts geometries. The Open Torque actuator is lightweight, however it is elongated in one direction, limiting the maximum degrees of freedom that can fit in a small robot. Moreover, most of the parts are 3d printed and thus can easily fail when exposed to high forces, or lose their properties when exposed to elevated temperatures. The solution presented in this article is a small actuator for sub 5 kg quadruped robots. The motor module is based on a hobby drone brushless motor [15] and a replaceable gearbox module. It integrates a custom brushless motor controller running Field Oriented Control (FOC) for superior torque control. It is capable of high torque bandwidth thanks to a rigid gearbox structure and low gear ratio. All aluminum parts of the module can be manufactured on a regular 3-axis milling machine. The main solution is directed towards quadrupedal robots, although other modular actuators proved to be useful in haptic devices and two-legged robots as well [16].

2. STANDALONE BRUSHLESS MOTOR MODULE

The actuator is described in all three aspects: mechanical, electrical and software design. The first section explains the mechanical design and motor selection process. Next, the motor controller PCB is described with the most important components specifically selected for the brushless actuator unit. The last section refers to the software features implemented in the controller, as well as calibration processes crucial for proper operation.

2.1. Mechanical design

The actuator (Fig. 1) is 50 mm in diameter, 37 mm in height, and weighs approximately 205 g. It consists of three main sections, which screwed together form a solid shell for the motor, gearbox, and controller electronics.
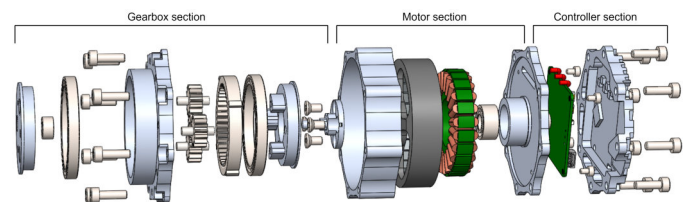

Fig. 1. Exploded view of the actuator

Starting from the back side, there is an enclosure cap for the electronics, serving as a radiator for the MOSFET transistors, MOSFET driver, and the motor. The IC's are heatsinked to the cap through a thermally conductive pad. The cap is directly connected to a part on which the motor's stator is press-fitted, and the controller PCB is mounted. Next, there is a distance cylinder with threaded holes to which the rest of the motor parts are screwed to. The cylinder can be customized based on the height of the motor used in the module. On the top of the module there is a part containing the gearbox. It is designed to be replaceable, allowing for changing the gearbox type. Currently, it is equipped with a single-stage 4.5:1 planetary gearbox.

Each part was milled from PA6 aluminum stock. The material was chosen as it has good mechanical properties and can be milled easily. Only three out of seven parts require flipping the material between milling stages, so the overall complexity of the structure is rather low, which leads to lower manufacturing costs.

The bearings and planet gear pins are press-fitted into the structure, whereas the sun gear is milled with two grooves and press-fitted onto the motor shaft with two respective lobes, as the connection between these two parts has to withstand high shear stresses.

The motor was chosen based on a few different criteria. Four motors were initially chosen for comparison with similar rotor diameter and height. Then, the available motors were compared with each other based on their KV parameter, phase resistance, and mass. The KV parameter is widely used when describing hobby motors, as it specifies the speed constant in RPM per volt. It is possible to estimate the torque constant based on KV

2

Bull. Pol. Acad. Sci. Tech. Sci., vol. 70, no. 2, p. e141008, 2022

parameter as the two quantities depend on each other [17]:

$$K_t = \frac{3}{2} \cdot \frac{1}{\sqrt{3}} \cdot \frac{60}{2\pi} \cdot \frac{1}{KV'}. \tag{1}$$

The $\sqrt{1/3}$ factor is for transforming between line to line and phase (line to neutral) quantities, whereas the 3/2 factor indicates a sinusoidal brushless motor is considered.

K_t is used for calculating the motor constant (K_m):

$$K_m = \frac{K_t}{\sqrt{R}}, \tag{2}$$

where R is the line to-line resistance.

Finally, the coefficient of how well the motor materials are utilized is introduced, describing the motor constant per unit of mass.

The results are listed in Table 1:

Table 1

Motor parameters comparison

Motor name	Sunnysky X4108s [18]	QM5006 [19]	Turnigy 4822 [20]
Outer diameter (mm)	46.1	47.5	47.5
Mass (g)	113	87	100
Height (mm)	25.5	20	25
KV rating	380	350	690
Pole pairs	12	14	11
Torque constant (Nm/A)	0.0217	0.0236	0.0119
Motor constant (Nm/$\sqrt{W}$)	0.0440	0.0492	0.0371
Motor constant per 1 gram of motor mass	0.00039	0.00057	0.00037
Phase resistance (Ω)	0.122	0.115	0.052

The choice of QM5006 motor was dictated by the higher motor constant and motor constant per unit of motor mass with respect to other motors presented in the classification. Moreover, QM5006 had the lowest profile among all motors, which was a preferred feature. The real motor was tested to ensure the parameters were estimated correctly. The measured torque constant turned out to be $K_t = 0.028$ Nm/A, and the motor constant $K_m = 0.056$ Nm/$\sqrt{W}$. Moreover, the shape of the back-EMF (back electromotive force) waveform was sinusoidal, when the motor shaft was spun by an external motor. The sinusoidal shape of the back-EMF waveform is desired to minimize the torque ripple, when applying field-oriented control algorithm. Before placing the motor in the case, the stator was taken out of the original aluminum housing and the rotor was milled with four additional slots to reduce the mass.

2.2. Motor controller

The integrated controller is responsible for running the Field Oriented Control (FOC) as well as sending and receiving CANFD (Controller Area Network Flexible Data-Rate) commands.

The controller unit is STMicroelectronic's STM32G431RG microcontroller. It is equipped with a hardware math accelerator (CORDIC) and hardware filtering peripheral (FMAC) for even faster trigonometric calculations, filtering velocity and current measurements. Moreover, the microcontroller has a built-in CANFD peripheral used for high-speed communication and two independent ADCs for measuring phase currents. It communicates with a few different external peripherals and sensors. The diagram presented in Fig. 2 shows the structure of the system. The commands are received through CANFD bus. The transceiver serves as a voltage level translator between the differential CANFD physical bus and the microcontroller's ground-referenced output signals. The microcontroller generates PWM waveforms that are fed into the MOSFET driver with the built-in bootstrap circuit (DRV8323) that is responsible for switching the MOSFET-N transistors. The IC is also responsible for adding dead time periods to the PWM control waveforms to prevent shoot-through events (when both upper and lower MOSFET transistors are conducting) and detecting any possible faults. Low-side shunt resistors are used for sensing phase currents. The voltage drop on each shunt resistor is measured, amplified by the internal amplifier of the DRV8323 IC, and outputted to the microcontroller's ADC peripheral.
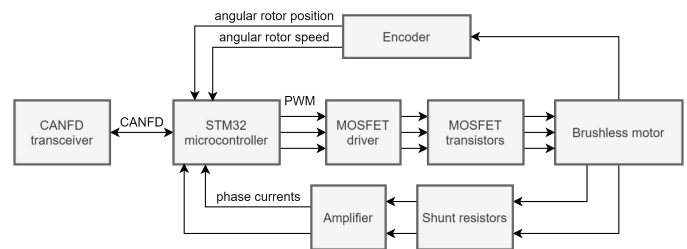

Fig. 2. Controller electronics structure

The diagram of the power supply unit is presented in Fig. 3.
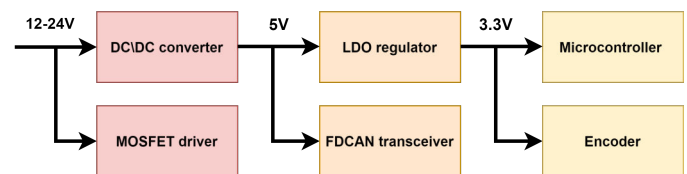

Fig. 3. Power supply diagram

The motor power supply can be in the range of 12 V to 24 V. As the devices on the 3.3 V bus can consume currents of up to 50 mA, a Low-Dropout regulator (LDO) would not be a sufficient choice due to excessive heating. That is why a DRV8323 IC was chosen with a built-in buck converter. The output of the converter was set to 5 V to power the CANFD transceiver. The 3.3 V bus is outputted by an LDFM ultra low dropout LDO which uses 5 V as its input voltage. This way, only about 1.7 V of voltage drop is present across the regulator, which results in no more than 0.1 W of power loss at the highest current consumption.

The DC bus is built out of eight ceramic 10uF capacitors. Ceramic capacitors were chosen as they feature low Equivalent Series Resistance (ESR) and small form factor. This way it was possible to make the low profile PCB case. The disadvantage of using ceramic capacitors in such applications is the DC bias derating [21], which was accounted for by adding extra capacitors according to the manufacturer's recommendations.

To measure the angular position and velocity of the motor's rotor, a magnetic 14-bit encoder AS5147 was used. It is able to output absolute position values through the SPI bus. For the speed measurement, the ABI output was used and connected to an internal STM32 encoder timer. The timer counts the time intervals between encoder increments (subsequent rotor positions) and filters the resultant velocity with a moving average filter. This approach is superior to position differentiation, especially at higher speeds, when the position changes by less than a bit between sampling instants. The sensor is sensitive to misaligned magnet placement, which can cause significant torque variations and should be accounted for with a calibration routine presented in the software paragraph.

The PCB is 33×33 mm in size and is capable of driving phase currents up to 40 A, depending on the used MOSFET transistors. It is optimized for high-frequency operation – the traces loops for charging and discharging MOSFET's gate capacitances were minimized. Moreover, the board is a four-layer design for improved interference immunity. Ceramic capacitors were placed as close to the switching transistors as possible. The ground is divided into power and digital planes, which are connected in a single point. This was done to minimize the influence of interference on the microcontroller, resulting from high currents flowing through the power section of the circuit. The PCB board is shown in Fig. 4.
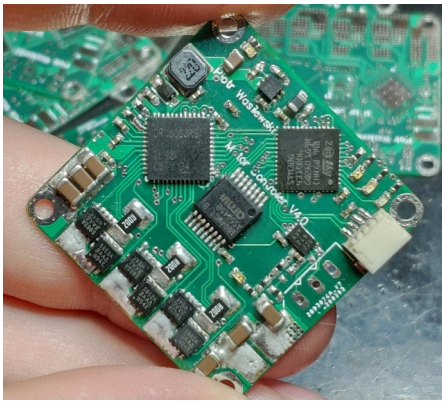

Fig. 4. Complete controller PCB

As stated earlier, the main purpose of the controller is running Field Oriented Control (FOC). This technique identifies three-phase AC currents as two orthogonal components fixed to the rotating rotor, greatly simplifying the mathematical analysis. It is widely used in applications requiring full torque at zero speed, dynamic motor behavior, and smooth performance over the full speed range.

FOC requires transforming from a stationary three-vector stator reference frame UABC to a rotating two-vector rotor ref-

erence frame UDQ0. This is done by introducing Park (3) and Clark (4) transformations [22].

$$T_C = \frac{\sqrt{3}}{2} \begin{bmatrix} 1 & -\frac{1}{2} & -\frac{1}{2} \\ 0 & \frac{\sqrt{3}}{2} & -\frac{\sqrt{3}}{2} \\ \frac{1}{\sqrt{2}} & \frac{1}{\sqrt{2}} & \frac{1}{\sqrt{2}} \end{bmatrix}, \tag{3}$$

$$T_P = \begin{bmatrix} \cos(\Theta) & \sin(\Theta) & 0 \\ -\sin(\Theta) & \cos(\Theta) & 0 \\ 0 & 0 & 1 \end{bmatrix}. \tag{4}$$

Forward transforms are used for current measurement purposes (5), whereas the inverses are used to set the desired voltages (6).

$$U_{ABC} = T_C T_P U_{DQ0}, \tag{5}$$

$$U_{DQ0} = (T_C T_P)^{-1} U_{ABC}. \tag{6}$$

This way, the three-phase AC variables were transformed into two non-sinusoidal D and Q components responsible for flux and torque production, respectively. After describing the transformations, it is necessary to introduce the equations governing a single pole pair motor in the d/q frame [23]:

$$V_q = RI_q + L_q \frac{dI_q}{dt} + \omega \lambda_r + \omega L_d I_d, \tag{7}$$

$$V_d = RI_d + L_d \frac{dI_d}{dt} - \omega L_q I_q, \tag{8}$$

where V_q, V_d are the applied voltages in each axis, R is the phase resistance, L_q is the inductance of the quadrature axis, L_d is the inductance of the direct axis, ω is the electrical angular speed and λ_r is the total rotor flux linkage. In permanent magnet machines, where magnets are placed on the surface of the rotor, the inductances in the q and d axes are roughly the same. These machines are called "non-salient" [17], as they produce torque only due to the permanent magnet flux, and no reluctance torque is present.

The $\omega \lambda_r$ term is usually called the "back-emf" term as it stands for the induced voltage due to the rotational velocity of the rotor. It is also the limiting factor for maximum velocity and can be mitigated in some limited range by making the $\omega L_d I_d$ term negative. It is done by setting the I_d current negative, which cancels out some of the induced voltage. This is defined as field-weakening action and although it is a solution for reaching greater speeds, the current applied in the d axis is transformed mostly to heat and effectively lowers the motor's torque constant. Moreover, drone motors usually have low inductance in d/q axes, which leads to high currents required to enable the field weakening feature. Even though the software of the controller is able to perform field weakening when higher speed is desired.

Due to the linear nature of equations (7) and (8), it is possible to utilize current control with two independent PI controllers.

4

Bull. Pol. Acad. Sci. Tech. Sci., vol. 70, no. 2, p. e141008, 2022

To improve their dynamic response, it is necessary to decouple both equations as they share common terms. This is done by the feedforward technique [24], and is noted as $V_{q\text{ff}}$ (9) and $V_{d\text{ff}}$ (10) in Fig. 5.

$$V_{q\text{ff}} = -\omega L_d I_d, \qquad (9)$$

$$V_{d\text{ff}} = \omega L_q I_q. \qquad (10)$$

After decoupling, the two axes are independent of each other and thus independent PI controllers can be applied.

The last block of the FOC control algorithm is the Space Vector PWM (SVPWM) modulator. It is responsible for modulating the waveforms in such a way that the DC bus is utilized in a more efficient manner and THD (Total Harmonic Distortion), as well as torque ripple, is reduced. Moreover, the modulation index of the SVPWM technique is 1.15 ($V_{\text{DCBUS}}/\sqrt{3}$), whereas the sine PWM modulation index is only 1 ($V_{\text{DCBUS}}/2$) [25]. This extends the linear region the motor controller can operate in.

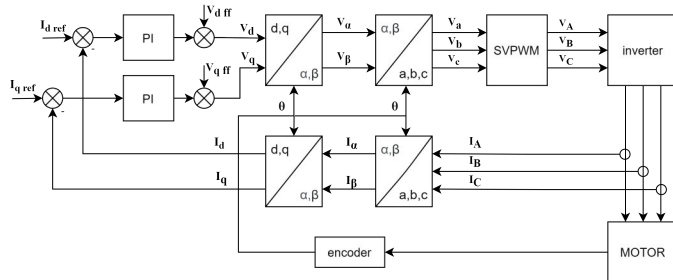The resulting FOC control algorithm is presented in Fig. 5.

Fig. 5. FOC algorithm for controlling currents in both q and d axes

$I_{d\text{ref}}$ and $I_{q\text{ref}}$ are two input quantities (expressed in amperes) responsible for field weakening and torque production, respectively. Generally, at low speeds the $I_{d\text{ref}}$ is kept at 0, whereas the $I_{q\text{ref}}$ is varied to affect the torque produced by the motor. The reference values are fed into the PI controller blocks, which calculate the voltages that have to be applied in each axis. After adding the feedforward terms, the quantities are transformed into three sinusoidal components through inverse Clark–Park transformation. Voltages V_α and V_β and currents I_α and I_β represent the 3-phase quantities (subscript A, B, C) in stator reference frame which consists of two axis – α and β. This is used as a temporary transformation between the stator and rotor reference frames. The last step is SVPWM modulation, and the resulting waveforms are fed into the motor. The feedback path is constructed with forward Clark–Park transform transforming the measured 3-phase currents and the resulting quantities are I_d and I_q. The encoder is used to determine the angular position of the rotor necessary for the transformations.

3. SOFTWARE

The software is divided into two separate sections – the bootloader and the motor application. The bootloader is placed at the beginning of the flash memory and allows for easy firmware updates through the CANFD bus, without the need of using an external programmer. The bootloading procedure is shortly described at the end of this section. The main firmware of the controller is responsible for running the FOC algorithm and receiving/sending CANFD messages. All FOC-related calculations are performed in the main 40 kHz timer interrupt. A single cycle of reading phase currents and rotor position, performing forward/inverse calculations, SVPWM modulation, and finally setting the voltages takes approximately 21 us. The controller's firmware is capable of measuring the motor's parameters such as electrical offset, magnet – encoder misalignment, d/q axis inductance, and phase resistance. All parameters are saved in the internal nonvolatile FLASH memory. Moreover, the controller stores its CANFD ID number, pole pair count, gear ratio, and eccentricity lookup tables in FLASH memory, so that the calibration process can be performed only once per module.

3.1. Electric position offset
Correctly measured position offset is crucial for the proper functioning of the actuator module. The controller commands a nonzero current on the d axis and fixes the theta angle (used for calculations) to 0. When the rotor position settles, the encoder position measurement is made and saved as an offset value. This way the controller knows the zero position at all times. The measured offset is saved in the nonvolatile memory region, ensuring the calibration result can be used in the next power-up cycle.

3.2. Magnet-encoder misalignment
Accounting for magnet misalignment is essential, especially on machines with many pole pairs. Slight misalignment may cause severe torque variations within a single rotation as the error is multiplied by the pole pair count. The eccentricity is measured by slowly rotating the rotor in both directions for a single rotation period. The resulting position read from the encoder is recorded and compared to the ideal position command. The error is then filtered with a low pass filter, averaged (from two-direction data) and a lookup table is constructed. It serves as an error reference that is used when the rotor position is calculated.

3.3. Phase resistance and d/q axis inductance
Phase resistance is measured by commanding a voltage step and measuring the steady-state current. The current has to be low enough not to heat up the windings and high enough to be accurately measured by shunt resistor sensors.

Inductance is estimated by measuring the rise time of the current when a small voltage step is applied in each axis. First, the rotor is aligned with the d or q axis. Then a small voltage step is applied, and the resulting current response is monitored to a point when it reaches 63.2% of the steady-state current. The steady-state current is calculated from the phase resistance measured beforehand. Inductance is calculated from the time constant and phase resistance. The voltage step is approximated by a PWM waveform of frequency high enough to not influence the step response (40 kHz).

Bull. Pol. Acad. Sci. Tech. Sci., vol. 70, no. 2, p. e141008, 2022

5

3.4. VBUS protection

The module is able to monitor and keep the DCBUS voltage in the desired range to protect the transistors, capacitors, and the driver IC from damage. The bus is sampled on each timer interrupt and if the voltage exceeds the threshold voltage a nonzero d-axis current is commanded to dump the energy into the motor. This is especially useful when the motor is commanded to stop or to go reverse, when it is rotating at high speed. This solution is superior, as it requires no additional components such as breaking resistors, however, may result in faster motor overheating in case of frequent breaking events.

3.5. Bootloader

A Python PC app is used for updating the device's firmware through CANFD bus. When initiated, the device is software-reset into bootloader mode. In bootloader mode, the microcontroller's memory is erased, and a new memory image is written. The communication is validated by CRC code after each 32-byte chunk of data. Updating the firmware through CANFD is advantageous, as it does not require a programmer, and can be performed using the main computer controlling the actuator. This way, the operator is capable of updating all actuators connected to the CANFD bus without any physical interaction (connecting the programmer between modules).

4. RESULTS

The complete motor module prototype is presented in Fig. 6.

Fig. 6. Complete actuator module

Several experiments were conducted to confirm the simulated results and expected actuator behavior. The internal controller variables were read directly from the microcontroller's memory. Manual measurements of d/q axis inductance and phase resistance were performed and compared to the automatically measured values by the controller itself.

4.1. d/q PI controller decoupling

The coupling effect could be observed when the motor is spun with a positive q-axis current, and then the current is reversed or any other change in the desired q-axis current occurs (7)-(8). During testing, the motor is able to rotate freely (Fig. 7).
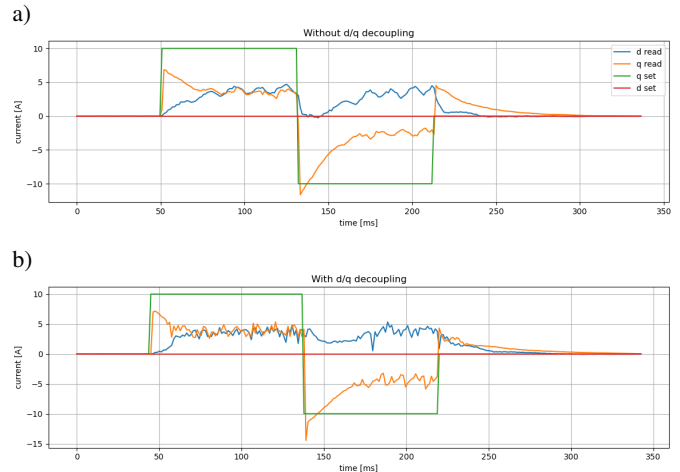
a)

b)

Fig. 7. d/q current response before (a) and after (b) the decoupling technique

Although the current response is less smooth (Fig. 7b), the d-axis readout current is less affected by a substantial change in q-axis current in comparison to Fig. 7a.

Similar behavior can be observed when running the GECKOCircuits [26] simulation as shown in Fig. 8.
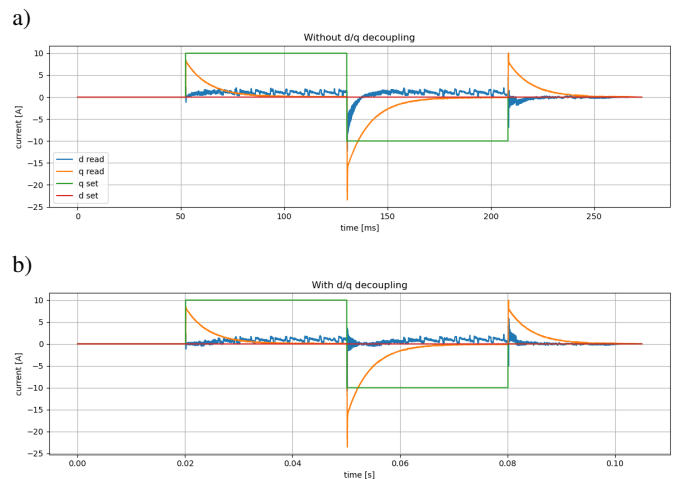
a)

b)

Fig. 8. d/q current response before (a) and after (b) the decoupling technique – simulation

The read d/q axis currents are not achieving the setpoint currents, as the motor starts rotating. When maximum speed for a given DC bus voltage is achieved, it is no longer possible for the current to flow, as the induced voltage is equal to the supply voltage. During the experiment, one can observe a negative spike in d-axis read current, when a sudden change in q-axis current occurs while the motor is spinning and no decoupling technique is implemented (Fig. 8a). However, after implementing the decoupling technique (Fig. 8b), the d-axis read current is much less affected, when q-axis current changes rapidly. Although the decoupling effect is rather limited, it should be noted that the motor is a low inductance one. In the case of utilizing a higher inductance motor, the coupling effects can be substantial.

6

Bull. Pol. Acad. Sci. Tech. Sci., vol. 70, no. 2, p. e141008, 2022

4.2. Motor parameters identification

Motor parameters such as d/q axis inductance and phase resistance were measured manually using a method proposed in [27]. The results were compared to those obtained from automatic measurements performed by the module. Values presented in Table 2 are averaged from 10 manual and automatic attempts.

Table 2
Comparison of manually obtained and automatically identified motor parameters

Name of the measured quantity	Manual measurement	Automatic measurement
Phase resistance [mΩ]	$122.9 \pm 9.26e-4$	$118.2 \pm 2.54e-4$
D axis inductance [µH]	$34.4 \pm 1.02e-6$	$32.9 \pm 1.41e-6$
Q axis inductance [µH]	$48.9 \pm 1.58e-6$	$40.8 \pm 6.72e-5$

It is crucial to note that the motor temperature has a significant influence on the parameters that are being identified, as the increased temperature changes the winding resistance [28]. Although the motor is a surface-mount permanent magnet motor, a slight difference in d/q axis inductance can be noticed. Moreover, the automatically identified q-axis inductance varies by roughly a few µH in respect to manual measurement. This is most probably caused by the fact that a nonzero q-axis current results in torque, which can move the rotor if not fixed rigidly, and influence the measurement outcome. Even though, the automatic identification is accurate enough for PI currents controllers tuning and can be used to automatically adjust controller gains to different motors.

4.3. Encoder eccentricity correction

The results of the calibration process are shown in Fig. 9. The data was collected on a setup with a radially misaligned magnet with respec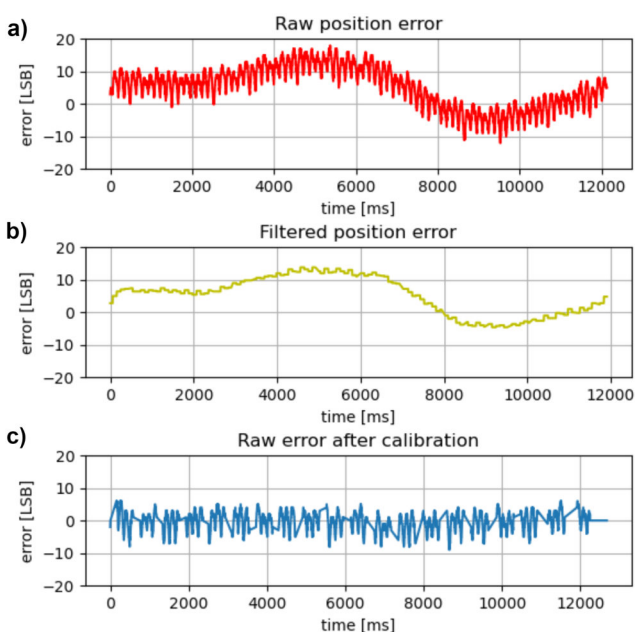t to the magnetic encoder. During the test, the rotor was slowly rotated by the controller in open-loop mode. The d axis was commanded with a non-zero voltage to produce d axis current needed for rotor alignment with the rotating magnetic field. Figure 9a is the raw error between the desired and actual position – the cogging torque is clearly visible and should be filtered out. Figure 9b depicts the error values after filtering with a low pass filter – at this point it is saved as a 128-point lookup table with reference error values. Finally, Fig. 9c shows the results of the calibration process – the error (including cogging) is within the ± 5 LSB margin.

4.4. Static torque measurement

The actuator was tested to determine its maximum torque capability and torque constant. The test stand used in the experiment was equipped with a 0–5 Nm torque sensor and a single motor module. One side of the sensor's shaft was fixed to the motor shaft, whereas the other was fixed to the test stand table (Fig. 10).
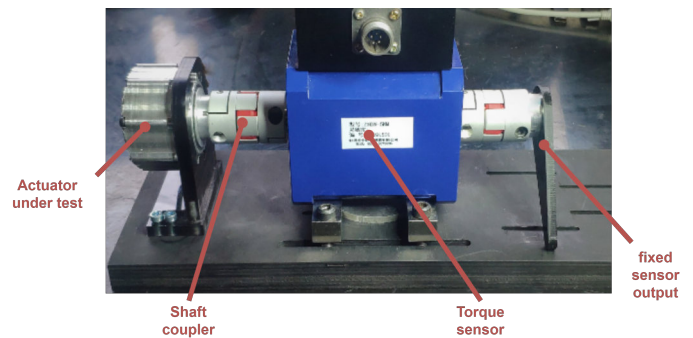

Fig. 10. Torque test bench

The motor was manually commanded with increasing q-axis current values, and after each try it was cooled down to a temperature of 25°C to minimize the influence of increased temperature, especially at high phase currents. The results are presented in Fig. 11.
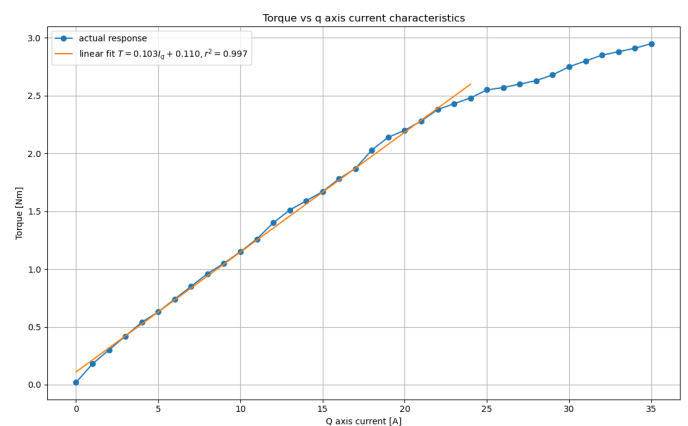

Fig. 11. Torque vs q-axis current characteristics

Up to 22 A of phase current, the static torque response can be described as linear with a coefficient of determination of

Fig. 9. Position error before (a, b) and after calibration (c)

Bull. Pol. Acad. Sci. Tech. Sci., vol. 70, no. 2, p. e141008, 2022

7

P. Wasilewski and R. Gradzki

0.997. However, at currents higher than 22 A of q-axis current the mo- tor's magnetic circuit starts to saturate. In order to achieve a linear torque response over the saturation region, the q-axis current should be increased in a nonlinear fashion to match the desired torque response. The peak torque of the module is 3Nm, and the torque constant in the linear region is roughly 0.103 Nm/A.

4.5. Thermal characteristics

The assumption during the thermal tests of this article's actuator was to command a certain amount of torque and wait for the temperature to settle. The maximum allowed temperature was 65°C. Figure 12 depicts the results of six different trials.
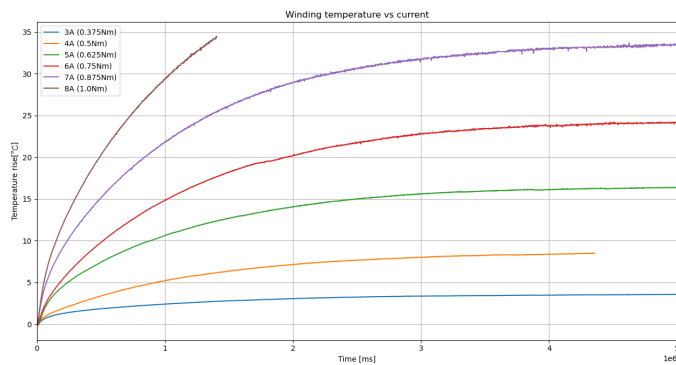

Fig. 12. Measured thermal characteristics of the module at different torque values

It was determined that the motor is able to produce 0.875Nm of continuous torque, without reaching the thermal limit of 65°C. Each test began from 30°C actuator temperature and 25°C ambient temperature.

5. CONCLUSION AND FUTURE WORK

The article presents the research conducted during modular actuator development and specific brushless motor parameter identification routines (phase resistance, d/q axis inductance). The actuator was designed to be modular, lightweight (210 g) and mechanically robust. Its form factor allows for usage in legged robot applications of total weight below 5 kg. Moreover, it has good torque to weight ratio and high maximum torque bandwidth (1kHz). The module was implemented with a custom control system and a high-speed CANFD communication bus that allows for high-frequency control routines, especially crucial for legged locomotion. Motor parameters identified by the integrated controller are used for current PI controllers tuning purposes. It is done to compensate for slight changes in hardware (phase resistance, inductance) that may occur when motors from different batches are used. The module is cost-efficient and easy to manufacture.

The actuator presented in the article is intended for use in a small (approx. 30×22 cm, < 5 kg) four-legged robot. It was implemented in both the 3D model and a real single leg prototype (Fig. 13).
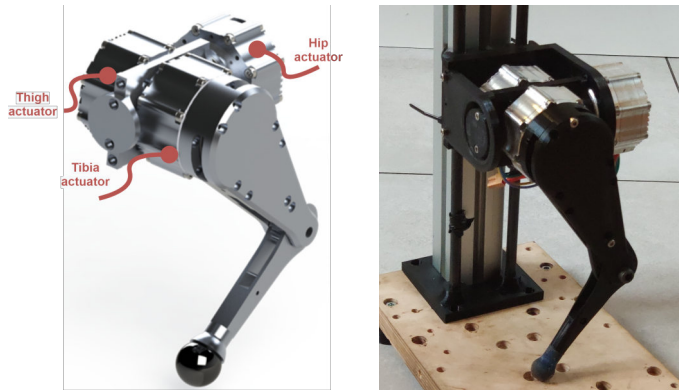

Fig. 13. Half of the robot's drivetrain

The limb drivetrain design is very compact. The hip actuator's output is directly coupled to the thigh motor. In order to keep all three joints independent, the tibia motor was placed on the thigh motor's output and it is coupled to the knee joint using an HTD 3 pulley belt. This way, the majority of the robot's mass is concentrated close to the body, effectively lowering the limb inertia.

Future work on the module includes thermal throttling, which is going to be implemented for temperatures exceeding a certain level to prevent burnout events. The mechanical durability of the modules is going to be examined on a vertical stand with linear rails. A single leg mounted to the cart is going to perform repetitive jumps, exposing the gearbox elements to high stresses, especially the press-fitted sun gear which is believed to be the weakest element of the structure.

REFERENCES

[1] C. Semini, N. Tsagarakis, E. Guglielmino, M. Focchi, F. Cannella, and D. Caldwell, "Design of HyQ -a hydraulically and electrically actuated quadruped robot," *Proceedings of the Institution of Mechanical Engineers. Part I: Journal of Systems and Control Engineering*, vol. 225, no. 6, pp. 831–849, 2011, doi: 10.1177/0959651811402275.

[2] M. Raibert, K. Blankespoor, G. Nelson, and R. Playter, "Bigdog, the rough-terrain quadruped robot," *IFAC Proc.*, vol. 41, no. 2, pp. 10822–10825, 2008, doi: 10.3182/20080706-5-KR-1001.01833.

[3] Boston dynamics company webpage. [Online]. Available: https:// www.bostondynamics.com. [Accessed: 08.11.2021].

[4] DailyMail. "Boston Dynamics robot dog inspects SpaceX site Texas." [Online]. Available: https://www.dailymail.co.uk/sciencetech/article-8458885/Boston-Dynamics-robot-dog-inspects-SpaceX-site-Texas.html. [Accessed: 08.11.2021].

[5] BBC news. "Coronavirus: Robot dog enforces social distancing in Singapore park." [Online]. Available: https://www.bbc.com/news/av/technology-52619568. [Accessed on 08.11.2021].

8

Bull. Pol. Acad. Sci. Tech. Sci., vol. 70, no. 2, p. e141008, 2022

[6] S. Seok, A. Wang, C.M. Yee, D. Otten, J. Lang, and S. Kim, "Design principles for highly efficient quadrupeds and implementation on the MIT Cheetah robot," *International Conference on Robotics and Automation*, Karlsruhe, Germany, 2013, pp. 3307–3312, doi: 10.1109/ICRA.2013.6631038.

[7] MIT Biomimetic Robotics Lab. "Optimal actuator design." [Online]. Available: https://biomimetics.mit.edu/research/0b02d0a6-b0d3-4011-bd95-183264a30217 [Accessed on 14.03.2021].

[8] P.M. Wensing, A. Wang, S. Seok, D. Otten, J. Lang, and S. Kim, "Proprioceptive actuator design in the MIT Cheetah: Impact mitigation and high-bandwidth physical interaction for dynamic legged robots," *IEEE Trans. Robotics*, vol. 33, no. 3, pp. 509–522, 2017, doi: 10.1109/TRO.2016.2640183.

[9] M. Hutter, C. Gehring, D. Jud, A. Lauber, C.D. Bellicoso, V. Tsounis, J. Hwangbo *et al.*, "ANYmal – a highly mobile and dynamic quadrupedal robot," *International Conference on Intelligent Robots and Systems (IROS)*, Daejeon, Korea (South), 2016, pp. 38–44, doi: 10.1109/IROS.2016.7758092.

[10] Unitree, "A1 actuator". [Online]. Available: https://www.unitree.com/components/a1_motor. [Accessed on 14.03.2021].

[11] B.G. Katz, "A low cost modular actuator for dynamic robots," M.A. thesis, Massachusetts Institute of Technology, June 2018.

[12] S. Seok, A. Wang, D. Otten, and S. Kim, "Actuator design for high force proprioceptive control in fast legged locomotion," *International Conference on Intelligent Robots and Systems*, Vilamoura-Algarve, Portugal, 2012, pp. 1970–1975, doi: 10.1109/IROS.2012.6386252.

[13] F. Grimminger *et al.*, "An open torque-controlled modular robot architecture for legged locomotion research," *IEEE Rob. Autom. Lett.*, vol. 5, no. 2, pp. 3650–3657, 2020, doi: 10.1109/LRA.2020.2976639.

[14] P. Wasilewski and J. Tołstoj-Sienkiewicz, "Modeling and simulation of a parallel quadruped robot," *20th International Carpathian Control Conference (ICCC)*, Poland, 2019, pp. 1–5, doi: 10.1109/CarpathianCC.2019.8765958.

[15] P. Wasilewski, M. Klimowicz, and R. Grądzki, "Design and analysis of state vector modulation based brushless motor driver," *AIP Conference Proceedings*, vol. 2029, p. 020078, 2018.

[16] D. Kim, S.J. Jorgensen, J. Lee, J. Ahn, J. Luo, and L. Sentis, "Dynamic locomotion for passive-ankle biped robots and humanoids using whole-body locomotion control," *Int. J. Rob. Res.*, vol. 39, no. 8, pp. 936–956, 2020, doi: 10.1177/0278364920918014.

[17] J.R. Mevey, "Sensorless field oriented control of brushless permanent magnet synchronous motors" M.A. thesis, Kansas State University, 2009.

[18] Himodels company, "Sunnysky 4108 product page." [Online]. Available: http://www.himodel.com/m/electric/SUNNYSKY_X4108S_380KV_Outrunner_Brushless_Motor_for_Multi-rotor_Aircraft.html. [Accessed 08.11.2021].

[19] Gearbest, "QM5006 product page." [Online]. Available: https://www.gearbest.com/motor/pp_09620387106.html [Accessed 08.11.2021].

[20] Hobbyking company. "Turnigy 4822 product page". [Online]. Available: https://hobbyking.com/en_us/turnigy-multistar-4822-690kv-22pole-multi-rotor-outrunner.html?_store=en_us. [Accessed 08.11.2021].

[21] M.D. Waugh, "Design solutions for dc bias in multilayer ceramic capacitors." [Onlione]. Available: http://www.compel.ru/wordpress/wp-content/uploads/2014/01/Mark-D.-Waugh.pdf [Accessed: 08.11.2021].

[22] T. Liu, Y. Tan, G. Wu and S. Wang, "Simulation of PMSM vector control system based on Matlab/Simulink," *International Conference on Measuring Technology and Mechatronics Automation*, Zhangjiajie, China, 2009, doi: 10.1109/ICMTMA.2009.117.

[23] M. Marufuzzaman, M.B.I. Reaz, M.S. Rahman, and A.M. Ali, "Hardware prototyping of an intelligent current DQ PI controller for FOC PMSM drive," *International Conference on Electrical & Computer Engineering (ICECE 2010)*, Dhaka, Bangladesh, 2010, pp. 86–88, doi: 10.1109/ICELCE.2010.5700559.

[24] A. Zentai and T. Daboczi, "Improving motor current control using decoupling technique," *EUROCON 2005 – The International Conference on "Computer as a Tool"*, Serbia, 2005, pp. 354–357, doi: 10.1109/EURCON.2005.1629934.

[25] M.N. Gujjar and P. Kumar, "Comparative analysis of field oriented control of BLDC motor using SPWM and SVPWM techniques," *2nd IEEE International Conference on Recent Trends in Electronics, Information Communication Technology (RTE-ICT)*, India, 2017, pp. 924–929, doi: 10.1109/RTEICT.2017.8256733.

[26] A. Musing and J.W. Kolar, "Successful online education – GeckoCIRCUITS as open-source simulation platform," *2014 International Power Electronics Conference (IPEC-Hiroshima 2014 – ECCE ASIA)*, Japan, 2014, pp. 821–828, doi: 10.1109/IPEC.2014.6869683.

[27] V. Bobek, "PMSM electrical parameters measurement". Freescale Semiconductor Aplication Note, Physics Forums, no. AN4680, 2013.

[28] D.Y. Ohm, *Dynamic model of pm synchronous motors*, Drivetech, Inc., Blacksburg, Virginia, 2000.